Continuous Electrochemical Heat Engines

Journal:	*Energy & Environmental Science*
Manuscript ID	EE-ART-04-2018-001137.R2
Article Type:	Paper
Date Submitted by the Author:	05-Jul-2018
Complete List of Authors:	Poletayev, Andrey; Department of Materials Science & Engineering, Stanford University; Stanford Institute for Materials and Energy Sciences, SLAC National Accelerator Laboratory McKay, Ian; Department of Chemical Engineering, Stanford University Chueh, William; Department of Materials Science & Engineering, Stanford University; Stanford Institute for Materials and Energy Sciences, SLAC National Accelerator Laboratory; Stanford University Precourt Institute For Energy Majumdar, Arunava; Stanford University, Mechanical Engineering; Stanford University Precourt Institute For Energy

SCHOLARONE™
Manuscripts

Broader Impact Statement:

The United States alone rejects over 60% of its primary energy intake as heat, at a variety of temperatures above ambient. Harvesting the rejected heat efficiently can meaningfully contribute to reducing carbon emissions. Here we propose continuous electrochemical heat conversion as a direct method of harvesting heat to electricity. Using flow cells and solid-oxide cells respectively, we build proof-of-principle heat harvesters operating both near ambient conditions, and at high temperatures. Importantly, electrochemical heat engines can use any redox-active fluids, including gases, not just ones directly conducting electrical charge, and do not rely on fixed-temperature phase transitions. We show that the geometry of electrochemical cells yields to optimization of power and efficiency, and lets us sidestep the constraints of cycle-based and thermoelectric direct heat harvesters. High efficiencies and relevant power densities are both achievable for continuous electrochemical heat engines.

TOC graphic:

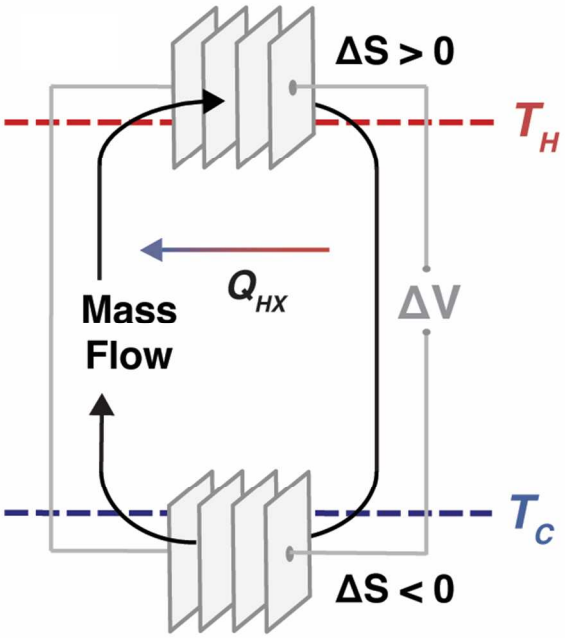

TOC sentence:

Direct electrochemical heat engines enable the use of novel redox-active fluids and optimization of both power and efficiency for broad-spectrum heat harvesting.

Title: Continuous Electrochemical Heat Engines

Authors: Andrey D. Poletayev[1,4†], Ian S. McKay[2†], William C. Chueh[1,4,5*], Arun Majumdar[3,5*]

Affiliations: [1]Department of Materials Science and Engineering, [2]Department of Chemical Engineering, [3]Department of Mechanical Engineering, Stanford University, Stanford CA 94305 (USA) [4]Stanford Institute for Materials and Energy Sciences, SLAC National Accelerator Laboratory, Menlo Park CA 94025 (USA) [5]Stanford Precourt Institute for Energy, Stanford CA 94305 (USA)

[†]These authors have contributed equally to this work

[*]Correspondence to: wchueh@stanford.edu, amajumdar@stanford.edu

Abstract: Given the large magnitude of exergy in waste heat, its efficient conversion to electrical power offers a significant opportunity to lower greenhouse gas emissions. However, it has been difficult to optimize the performance of new direct energy conversion approaches because of the coupling between entropy change and thermal and electrical transport in continuously operating devices. With electrochemical cells driving flowing electrolytes in symmetric redox reactions at different temperatures, we demonstrate two continuous electrochemical heat engines that operate at 10–50 ºC and at 500–900 ºC, respectively. Simulations of kilowatt-scale systems using electrochemical cells stacked in series suggest efficiencies over 30% of the Carnot limit and areal power densities competitive with solid-state thermoelectrics at maximum power. Although entropy change, thermal transport and electrical transport are inherently coupled in solid-state thermoelectrics, they can be somewhat circumvented in electrochemical systems, thus offering new opportunities to engineer efficient energy conversion systems.

Main Text: Roughly 90 percent of the world's usable power is produced thermally before being converted by heat engines into useful work[1,2]. Given that the efficiency of automobile engines falls in the range of 20-50% and that of combined-cycle gas turbines for large-scale stationary power is roughly 60%[3], the United States rejects over 60 percent of its primary energy use as waste heat[4], at a wide range of temperatures above ambient. Large quantities of heat produced by energy-intensive manufacturing processes also remain unutilized[5]. With over 300 GW of power theoretically extractable in the US alone[6], converting this waste heat directly to electricity could lead to economic and environmental benefits as well as reduced carbon emissions.

Fundamentally, a direct thermal-to-electric heat engine converts entropy to an electric potential, while allowing charge transport and irreversible thermal parasitics. The intensive properties responsible for the three processes are thermopower α, thermal conductivity κ, and electrical resistivity ρ. Thermoelectric (TE) heat engines, together with thermogalvanic (TG) analogues[7–9], are widely considered to be the most promising candidates for converting distributed heat sources to electricity[10–14]. For all, the optimization of device efficiency and maximum power reduces to the figure of merit $z=\alpha^2/\kappa\rho$ composed exclusively of the intensive properties of one material although the geometry and sizes of the elements also determine their performance[15–17]. Since these material properties are often coupled, the optimization of z is inherently constrained. This constraint has made it difficult to compete with traditional

thermofluid cycles[13], and therefore limited their adoption in practical systems. Electrochemical sodium heat engines, which have demonstrated high efficiency and reasonable scalability, have stringent temperature requirements and stability issues[18–20] because of their reliance on a specific high-temperature phase transition. Thermally regenerative electrochemical systems allowing long-cycle intermittent operation[21–25] have received additional attention. Heat conversion using steady-state fluid-phase redox reactions has been partially conceptualized[24,26–29], and temperature-dependent properties of redox couples studied extensively[9,26,30–32]. However, a demonstration of a continuously operating heat harvesting electrochemical system, e.g. with appropriate hot and cold terminals and recuperative heat exchange, has not yet been put forth. Thus, the main challenge in direct heat-to-electricity conversion is to experimentally realize continuous thermodynamic cycles that sidestep the coupling of entropy, heat and charge transport and operate across a broad range of temperatures.

In this work, we leverage the progress in redox flow batteries and fuel cells to experimentally demonstrate continuous electrochemical heat engines based on two redox-active working fluids separated by ion-selective membranes. In a continuous cycle, a stack of electrochemical cells runs a redox reaction at a hot temperature T_H, gaining entropy, while another simultaneously runs the reverse reaction at a cold temperature T_C, expelling entropy (Figure 1a). The redox reactions occur such that charge neutrality is achieved via ion transport through ion-selective membranes in the cells. Because the potentials for these redox pair reactions are temperature dependent, a potential difference is also produced between T_H and T_C when the cells are connected in series via external leads. This potential difference combined with electron flow produces electrical power, making this system a continuous electrochemical heat engine. In addition to the charge flow loop between the sets of redox reactions at T_H and T_C, there is also a closed mass flow circuit. The fluid electrolytes carrying redox species on either sides of the membranes flow in separate mass-flow loops between T_H and T_C. In between these two thermal reservoirs, the respective hot and cold streams exchange heat through recuperative heat exchangers.

To further outline the operation of these heat engines, first consider a cyclical, rather than continuous, mode of operation, similar to regenerative cycles based on intercalation chemistry[21–24], subject to the constraint of equal flow rates of fluid electrolytes. It would proceed in two steps, as in Figure 1b. Start with electrochemical cells at T_C charged, electrochemical cells at T_H discharged, and with electrical leads disconnected. At this point, no heat flows between T_H and T_C through our system, and no power is generated. First, connect cells with electrical leads, discharge cells at T_C, and charge the cells at T_H. Next, open the electrical circuit, and flow the redox fluids through the heat exchanger. Recuperative heat exchange between the reduced and oxidized fluid streams decreases irreversible heat loss between hot and cold temperature reservoirs. Power is generated in the first step, while irreversible heat leaks occur in the second; the efficiency is only limited by the efficiency of the heat exchanger in the quasi-reversible limit of negligible current densities (Supplementary Materials). As the duration of every separate step in the cycle approaches zero, continuous operation is achieved (Figure 1c). Based on the above device configuration, the overall heat engine efficiency is given as:

$$\eta = \frac{I\left(\Delta V_{OC} - I\left(R_C + R_H\right)\right) - I^2 R_{Lead} - P_{aux}}{IT_H\left(\alpha_1 - \alpha_2\right) + Q_{Loss} + \left(1 - \varepsilon_{HX}\right)\dot{m}c_p\Delta T} \quad (1)$$

where R_C and R_H are the total resistances of electrochemical cells at T_C and T_H respectively (Figure 2a), R_{Lead} is the resistance of the electrical leads, and P_{aux} is any auxiliary power input, such as a pump driving circulation. The thermodynamically reversible heat input Q_{Rev} is $IT_H(\alpha_1-\alpha_2)$ (Figure 2b). Heat leaks from the mass transport of reactants are $(1-\varepsilon_{HX})\,\dot{m}\,c_p\,\Delta T$, where ε_{HX} is the effectiveness of the recuperative heat exchanger and $\dot{m}$ the mass flow rates of the redox-active electrolyte fluids. Q_{Loss} reflects all conductive leaks in the system (Figure 2b). Common conductive heat leaks include leaks along leads (Q_{Lead}), walls of the heat exchanger (Q_{Wall}), and along the fluid if it is stagnant (Q_{Cond}, Supplementary Materials).

The parameter space for the optimization of power output and efficiency includes the mass flow rates $\dot{m}$, the engineering dimensions of the leads, cells, and heat exchangers, and the stacking of electrochemical cells in series at T_H and T_C. Unlike in TE systems, the large parameter space does not reduce to the intensive properties of one material. Electronic current flows between T_H and T_C only in electrical leads. Conversely, ionic current only flows in the solid-state membranes isothermally at T_H and T_C, not between T_H and T_C, while the working fluids do not contribute to net transport of electrical charge (near-infinite $R_{Fluid} >> R_{Lead}$, Figure 2a). The total electrical conductance of the heat engine depends only on the ion-conducting membrane and the catalytically active electrodes.

The optimization of thermal and electrical conductance over distinct system components is a departure from that in solid-state TE devices. Furthermore, heat flow between the hot and cold reservoirs in solid-state TE occurs by electrons and phonons, the latter often dominating the conductance and creating a parasitic shunt. Even if phonon conductance is suppressed, the electrical and thermal conductances of the electrons in solid-state materials are coupled in accordance with the Wiedemann-Franz law. In the current system, by contrast, heat flow between the hot and cold thermal reservoirs occurs via convective heat transfer of the electrolyte flowing between them. The flow of electrolytes, even if the latter are redox-active, carries no net charge, and is independent and decoupled from the ion-conductance and catalytic activity of the electrodes that control the electrical conductance. The use of a recuperative heat exchanger between the hot and cold fluid flow reduces heat losses to the environment, thereby allowing for higher efficiency (Figure 2b). Furthermore, unlike in TE or TG systems where each power-generating "leg" of the device conducts heat, electrochemical cells can be stacked in series at each temperature (Figure 1b-c, Figure 2a). For a device of cell area A operating at constant current density J per unit area of the electrochemical cells, the stacking of N cells, each of area A/N, in series, decreases the overall current I through the leads by a factor of N without affecting the overall power production. The reduction in the total device current allows the electrochemical heat engine to circumvent the Wiedemann-Franz law as it pertains to the electronic leads. We further detail and derive the optimization of heat leaks in the Supplementary Materials.

The proposed concept is highly generalizable. As we demonstrate below, the optimization of continuous electrochemical heat engines does not depend on phase transitions[20], variation of material parameters with temperature[12], temporal constraints, e.g. cycling rate[21,22], or fundamental trade-offs, e.g. the need for an electron crystal phonon glass[13]. Only the stability and kinetics of the redox fluid and the electrochemical cell set the cycle temperature, ranging from well below ambient[33,34] to ~1,000 °C[35].

The reversible entropy change of interface electrochemical reactions, ΔS, depends on a variety of factors, such as the solvation of the ions in different oxidation states [31,36,37]. A wide

range of species supporting redox processes can serve as the working fluids: liquids, gases, dissolved species and slurries. Expressed per coulomb of charge transferred, ΔS manifests as the electrochemical thermopower α; the difference of the thermopowers in the two redox reactions α_1-α_2 determines the open-circuit voltage (OCV) output of the device as $\Delta V_{OC} = |(\alpha_1-\alpha_2)\,\Delta T|$, where $\Delta T = (T_H-T_C)$. Table 1 lists the thermopower of individual liquid redox couples measured experimentally in this work, which allow for combined α_1-α_2 in excess of -3 mV K^{-1} (also shown in Figure 3a). To generate electricity, the heat engine voltage $V = \Delta V_{OC} - IR$ (where I is the current and R is the current-dependent resistance of both cells) must be positive at appreciable currents. This equation highlights the decoupling of carrier entropy and charge transport: while the redox fluids determine ΔV_{OC}, R is determined primarily by the electrochemical cells. Clearly, both the working fluids and system design for electrochemical heat engines represent vast and largely unexplored parameter spaces.

To demonstrate the generality and wide range of conditions amenable to this type of continuous electrochemical heat engine, we have built two proof-of-concept energy harvesters that operate in very different temperature regimes. For the low-temperature system, the aqueous $V^{2+/3+}$|| $Fe(CN)_6^{3-/4-}$ redox couples were chosen on the merits of their high charge capacity, facile redox behavior, and large $|\alpha_1-\alpha_2|$. For the high-temperature system, oxygen gas was used as an entropy carrier via the $H_2/H_2O||O_2$ couples, mediated by solid-oxide electrochemical cells. Figure 3 illustrates the dependence of cell potentials on temperature in the two systems.

Figure 4a shows the low-temperature electrolyte-circulated thermal energy harvester. The system comprised of two membrane-electrode-assembly flow cells and a two-channel counterflow heat exchanger (Figure S7). For T_H = 50 °C and T_C = 10 °C, Figure 4b shows the voltage generated across the two cells as a function of the current density flowing between the cells. The polarization curve yields an OCV of 108 mV and a maximum power density of 110 μW cm^{-2} at a voltage of 60 mV (Figure 4c) for cells of area 10 cm^2. The heat input into the energy harvester was calculated based on the thermodynamic heat input $IT_H(\alpha_1-\alpha_2)$ (15.0 mW), the energy input $\dot{m}c_p\Delta T$ into the two working fluids with specific heats c_p and mass flow rates $\dot{m}$ from the cold to the hot junction (45.5 mW) assuming no heat exchange. Neglecting heat loss to the ambient, and heat leaks along current collecting leads and the walls of the heat exchanger tubing, we estimate from the above experimental data an efficiency $\eta = 0.15\eta_c$ at the maximum power point, where the Carnot efficiency $\eta_c = (T_H - T_C)/T_H = 12.4\%$. We include all components of the calculation in Table S3. Since this estimate of efficiency is only approximate, we provide a rigorous calculation based on computational modeling of a scaled system that includes all the heat leak pathways below (Equation 1 and Figures 5-6). Because the electrolyte flow rate in both anolyte and catholyte were matched to the reaction rate in the small cells, the total flow rate was low, limiting the effectiveness of the heat exchanger and leaving room for improvement in system performance. Even so, our use of fast electron-transfer reactions harnessing large solvation entropies[31] yields power density under continuous operation that is ~100x higher than the cycle-averaged power density in intercalation-based thermally regenerative systems[21,22] on a per-area basis for the same temperature range. Further details on the liquid cells, efficiency calculations, and heat exchanger performance are provided in the Supplementary Materials.

Figure 4d shows the high-temperature thermal energy harvester, which uses oxygen as an entropy carrier with anode-supported Ni-YSZ/YSZ/$(La,Sr)MnO_{3-x}$ button cells (YSZ = yttria-stabilized zirconia) carrying out the water splitting reaction at T_H and the hydrogen combustion reaction at T_C in a two-zone vertical furnace (Figure S2). Figure 4e shows the polarization curve

and the resulting output power at T_H = 900 °C and T_C = 650 °C, and Figure 4f shows the maximum power densities as a function of T_C and T_H. For T_H = 900 °C, we obtained an OCV of 90 mV and a maximum power density of 0.32 mW cm^{-2} at a voltage of 50 mV. As expected, the resistance of the cold cell limits the power density for low T_C, and OCV limits power for smaller ΔT. This is in contrast to the liquid-phase demonstration, where only the freezing of the electrolyte and thermal stability of the chosen redox couples define the operational temperature range. We did not attempt to close the mass flow, instead exhausting the gases as they exited the chambers.

The high and low temperature demonstrations represent select points in the wide space open to the materials and system design of continuous electrochemical heat engines. To further explore this parameter space, we estimate the practical performance of continuous electrochemical heat engines using an analytical modeling framework. The simulation includes mass transport and solution resistance[38–41] as well as conductive heat leaks along the current collecting leads[18] and along the walls of a counter-flow heat exchanger. As reflected in Equation 1, these considerations account for all losses at the system level. The relevant performance metrics for continuous electrochemical heat engines are the maximum power and efficiency at the maximum power point.

Figure 5a shows the predicted efficiency versus output power density per area of membrane for a gas-phase electrochemical heat engine using oxygen gas as the entropy carrier, similar to our experimental demonstration in Figure 4. Figure 5a shows the efficiency (eq. 1) versus output areal power density for a gas-phase electrochemical heat engine using oxygen gas as the entropy carrier, parameterized by the operating current density J. At each value of J, the mass flow rates $\dot{m}$ of the electrolytes were varied to optimize overall device power output (numerator of equation 1) in a tradeoff between mass transport overpotentials and pumping power expenditures[42]. Increasing the overall thermal conductance of the heat exchanger by a factor of ten does not noticeably affect the maximum power output, but improves the efficiency at the maximum power point from 0.154η_c to 0.376η_c. Similar results are obtained for the liquid-based heat engine (Figure S8). This result illustrates the optimization of heat leaks independent of the electronic transport and entropy conversion in the heat engine. Figure 5b simulates the maximum output power per membrane area, and Figure 5c simulates the efficiency at maximum power for a continuous electrochemical heat engine with the heat exchanger rated for 20 W K^{-1}. In this simulation, output power densities over 40 mW cm^{-2} are possible, with efficiencies over 0.35η_c at the maximum power point. Similar to our experimental demonstration in Figure 4f, for fixed T_H and low T_C the power density is limited by the resistance of the low-temperature cells. These results indicate that improvements to the cell resistance (e.g., improved ionic transport or electrocatalysts) increase the power density and extend the operable temperature range of the engine for a given working fluid (Figure S3) without affecting entropy conversion or heat transport in the system.

An analysis of a generalized liquid-phase heat engine also points to two distinct operating regimes. For active species concentrations and temperatures corresponding to those in our proof-of-principle system (Figure 4), the maximum power increases with the electrode reaction rate constant k_0 until $k_0 = 0.05$ cm sec^{-1} (Figure 6a), achievable with a variety of redox couples. At higher values of k_0, the power output becomes only a function of thermopower α and insensitive to k_0. In this regime, the current-dependent polarization resistance for the surface reactions is smaller than the combined ohmic resistance of the cell membrane and mass transport losses in

solution. Since the electrochemical heat engine has four active interfaces, this result shows that a regime exists in which interfacial kinetics do not limit the performance of the system, despite the additional interfaces we introduce relative to solid-state thermoelectrics. Instead, such systems are limited by purely ohmic components and the properties of redox-active fluids. Ideal fluids for electrochemical heat engines will possess a high entropy of charge transfer and high concentrations of available redox species per unit mass. Figure 6b shows that efficiencies over 30% of η_c at the maximum power point are achievable for a wide range of electrochemical redox couples. As seen in a variety of other electrochemical systems[38,43], the simulation also suggests that mass transport limits the maximum obtainable power density; more efficient fluid flow patterns than the flat-plate geometry simulated here, and increased active species concentrations, will both lead to higher power densities. Figure 6c simulates the latter case, in which a heavily concentrated redox fluid is used (15 M, corresponding to pure substances or slurries[44,45]), enabling power densities over 20 mW cm^{-2}.

The system modeling in Figures 5-6 has been carried out using the parameters of published technologies and in absence of assumptions regarding the performance of electrochemical cells. The single unknown in the system is the choice of liquid-phase redox couples, for which reasonably fast kinetics, a high thermopower, and high concentrations of charge are simultaneously required. Since the majority of the thermopower derives from solvation effects rather than from inner-sphere rearrangements, we see no fundamental trade-off between these components of performance. [30,31,36,37] This is further in contrast to solid-state thermoelectrics, where a material's figure of merit *z* embodies the trade-offs inherent in solid-state optimization.

We have demonstrated two electrochemical heat engines operating in very different temperature regimes: a vanadium-ferrocyanide flow system harvesting low-temperature heat sources, and a hydrogen-oxygen flow system operating at much higher temperatures. While the working fluids presented here were not optimized for stability, many other redox couples (e.g. Table 1) are available, and further demonstrations will showcase a longer-lifetime system. We also note that improvements to the stability of flow batteries, fuel cells and electrolysis cells could also benefit our approach. Similarly, improvements to the areal power densities of these systems will benefit the power output of electrochemical heat engines. The operating temperature ranges for these systems are limited by the stability of the redox couple and the performance of the electrochemical cells, respectively. For practical applications, temperature-dependent solubility of redox couples, stability of electrolytes, reagent crossover and system-level economic feasibility will have to be addressed. Further research could also extend the operating temperature range of electrochemical heat engines, e.g. by combining proton-conducting oxide fuel cells around 600 °C on the hot side and polymer-electrolyte fuel cells near ambient temperature on the cold side to span this important temperature range. Importantly, our modeling shows that at a practical scale the doubled number of interfaces relative to TE and TG systems does not necessarily limit performance, as the added irreversibility is compensated by the increased thermopower and counterflow heat exchange. Based on system modeling, and accounting for practical losses (Equation 1 and Figures 5-6), the continuous electrochemical heat engine can scalably reach maximum power point efficiencies well over 30% of η_c under diverse operating conditions. Furthermore, the ability to form stacks of cells in series at each temperature to increase voltage without the coupling to heat losses is fundamentally different from that in TE systems: it enables further minimization of heat leaks while independently optimizing the electrical performance. It is also worth noting that stacks of multiple electrodes can achieve

much higher areal power densities than individual cells. For example, with 100 cells per stack (the geometry simulated in Figures 5-6), the device-level areal power density is 4 W cm^{-2}, a quantity that is more comparable with the areal power densities generally reported for TE devices.

By decoupling thermal and electrical entropy generation pathways, we demonstrate effective energy conversion in regimes heretofore inaccessible to TE, TG, regenerative, or other thermal-fluid heat engines. While electricity generation is demonstrated in this work, operating these systems in reverse could in principle enable electrochemical refrigeration as well. In addition to the significant flexibility in size and form, a vast parameter space exists for the optimization of working fluids: redox transformations of pure substances, ion-transporting liquids, and gas-phase reactants could all be used. With the development of suitable redox chemistries and flow systems, continuous electrochemical heat engines could fill a vital missing space in the existing landscape of energy harvesting technologies.

References and Notes:

1. The World Bank. *World Development Report 2011: Conflict, Security, and Development.* (2011).
2. Gur, I., Sawyer, K. & Prasher, R. Searching for a Better Thermal Battery. *Science (80-.).* **335,** 1454–1455 (2012).
3. U.S. Energy Information Administration. *Annual Energy Review*. (2012).
4. Lawrence Livermore National Laboratory. *USA 2015 Energy Flow Chart*. (2016).
5. *Waste Heat Recovery for the Cement Sector: Market and Supplier Analysis*. (2014).
6. Rattner, A. S. & Garimella, S. Energy harvesting, reuse and upgrade to reduce primary energy usage in the USA. *Energy* **36,** 6172–6183 (2011).
7. Hu, R. *et al.* Harvesting waste thermal energy using a carbon-nanotube-based thermo-electrochemical cell. *Nano Lett.* **10,** 838–46 (2010).
8. Abraham, T. J. *et al.* Towards ionic liquid-based thermoelectrochemical cells for the harvesting of thermal energy. *Electrochim. Acta* **113,** 87–93 (2013).
9. Quickenden, T. I. & Vernon, C. F. Thermogalvanic conversion of heat to electricity. *Sol. Energy* **36,** 63–72 (1986).
10. Dresselhaus, M. S. *et al.* New Directions for Low-Dimensional Thermoelectric Materials. *Adv. Mater.* **19,** 1043–1053 (2007).
11. Vineis, C. J., Shakouri, A., Majumdar, A. & Kanatzidis, M. G. Nanostructured thermoelectrics: big efficiency gains from small features. *Adv. Mater.* **22,** 3970–80 (2010).
12. Snyder, G. J. & Toberer, E. S. Complex thermoelectric materials. *Nat. Mater.* **7,** 105–14 (2008).
13. Bell, L. E. Cooling, Heating, Generating Power, and Recovering Waste Heat with Thermoelectric Systems. *Science* **321,** 1457–1461 (2008).

14. Majumdar, A. Thermoelectricity in Semiconductor Nanostructures. *Science* **303,** 777–778 (2004).

15. Heikes, R. R. & Ure, R. W. *Thermoelectricity: Science and Engineering*. (Interscience Publishers, 1961).

16. Goupil, C., Seifert, W., Zabrocki, K., Müller, E. & Snyder, G. J. Thermodynamics of Thermoelectric Phenomena and Applications. *Entropy* **13,** 1481–1517 (2011).

17. Kim, H. S., Liu, W., Chen, G., Chu, C.-W. & Ren, Z. Relationship between thermoelectric figure of merit and energy conversion efficiency. *Proc. Natl. Acad. Sci.* **112,** 8205–8210 (2015).

18. Hunt, T., Weber, N. & Cole, T. Research on the Sodium Heat Engine. *Proc. 13th Intersoc. Energy Convers. Eng. Conf.* 2011 (1978).

19. Weber, N. A Thermoelectric Device Based on Beta-Alumina Solid Electrolyte. *Energy Convers.* **14,** 1–8 (1974).

20. Cole, T. Thermoelectric energy conversion with solid electrolytes. *Science (80-.).* **221,** 915–20 (1983).

21. Lee, S. W. *et al.* An electrochemical system for efficiently harvesting low-grade heat energy. *Nat. Commun.* **5,** 3942 (2014).

22. Yang, Y. *et al.* Membrane-Free Battery for Harvesting Low-Grade Thermal Energy. *Nano Lett.* **14,** 6578–6583 (2014).

23. Zhao, D. *et al.* Ionic thermoelectric supercapacitors. *Energy Environ. Sci.* **9,** 1450–1457 (2016).

24. Chum, H. & Osteryoung, R. *Review of Thermally Regenerative Electrochemical Systems*. **1,** (1981).

25. McKay, I. S. & Wang, E. N. Thermal pulse energy harvesting. *Energy* **57,** 632–640 (2013).

26. Hammond, R. H. & Risen, W. M. An electrochemical heat engine for direct solar energy conversion. *Sol. Energy* **23,** 443–449 (1979).

27. Virkar, A. A. V. A., Weber, N. & Joshi, A. A. V. Theoretical assessment of an oxygen heat engine: the effect of mass transport limitation. *Energy Convers. Manag.* **32,** 359–370 (1991).

28. Johnson, L. G. & Muller, J. R. U. S. Patent No. 7,160,639. (2007).

29. Gerlach, D. W. & Newell, T. A. *An Investigation of Electrochemical Methods for Refrigeration*. **61801,** (2004).

30. Hupp, J. T. & Weaver, M. J. Entropic Driving-Force Effects upon Preexponential Factors for Intramolecular Electron Transfer: Implications for the Assessment of Nonadiabaticity. *Inorg. Chem.* **23,** 256–258 (1984).

31. Hupp, J. T. & Weaver, M. J. Solvent, Ligand, and Ionic Charge Effects on Reaction Entropies for Simple Transition-Metal Redox Couples. *Inorg. Chem.* 3639–3644 (1984).

32. Quickenden, T. & Mua, Y. A Review of Power Generation in Aqueous Thermogalvanic

Cells. *J. Electrochem. Soc.* **142,** 3985 (1995).

33. Zhang, C., Zhao, T. S., Xu, Q., An, L. & Zhao, G. Effects of operating temperature on the performance of vanadium redox flow batteries. *Appl. Energy* **155,** 349–353 (2015).
34. Ji, Y., Zhang, Y. & Wang, C.-Y. Li-Ion Cell Operation at Low Temperatures. *J. Electrochem. Soc.* **160,** A636–A649 (2013).
35. Hehemann, R. F., Mervin Ault, G. & Weir, J. R. High-Temperature Materials. *J. Electrochem. Soc.* **107,** 19C (1960).
36. Turner, J. W. & Schultz, F. A. Intramolecular and environmental contributions to electrode half-reaction entropies of M(tacn)(2)(3+/2+) (M = Fe, Co, Ni, Ru; tacn = 1,4,7-triazacyclononane) redox couples. *Inorg. Chem.* **38,** 358–364 (1999).
37. Turner, J. W. & Schultz, F. A. Solution characterization of the iron(II) bis(1,4,7-triazacyclononane) spin-equilibrium reaction. *Inorg. Chem.* **40,** 5296–5298 (2001).
38. Braff, W. a., Buie, C. R. & Bazant, M. Z. Boundary Layer Analysis of Membraneless Electrochemical Cells. *J. Electrochem. Soc.* **160,** A2056–A2063 (2013).
39. Braff, W. A., Bazant, M. Z. & Buie, C. R. Membrane-less hydrogen bromine flow battery. *Nat. Commun.* **4,** 2346 (2013).
40. Huskinson, B. & Aziz, M. J. Performance Model of a Regenerative Hydrogen Bromine Fuel Cell for Grid- Scale Energy Storage. *Energy Sci. Technol.* **5,** 1–16 (2013).
41. Huskinson, B. *et al.* A metal-free organic-inorganic aqueous flow battery. *Nature* **505,** 195–8 (2014).
42. Hoyt, N. C., Savinell, R. F. & Wainright, J. S. Modeling of flowable slurry electrodes with combined faradaic and nonfaradaic currents. *Chem. Eng. Sci.* **144,** 288–297 (2016).
43. Newman, J. & Tiedemann, W. Porous-electrode theory with battery applications. *AIChE Journal* **21,** 25–41 (1975).
44. Duduta, M. *et al.* Semi-solid lithium rechargeable flow battery. *Adv. Energy Mater.* **1,** 511–516 (2011).
45. Presser, V. *et al.* The electrochemical flow capacitor: A new concept for rapid energy storage and recovery. *Adv. Energy Mater.* **2,** 895–902 (2012).
46. Barin, I. *Thermochemical Data of Pure Substances*. (VCH, 1995).

Acknowledgments:

This work is supported by the Department of Energy, Laboratory Directed Research and Development funding, under contract DE-AC02-76SF00515, the Global Climate and Energy Project, and the Stanford Precourt Institute for Energy. I.S.M. was supported by the Department of Defense through the National Defense Science & Engineering Graduate Fellowship Program, and by the Fannie and John Hertz Foundation through a Hertz Foundation Fellowship. A. D. P. was supported by the National Science Foundation Graduate Research Fellowship and the Stanford Interdisciplinary Graduate Fellowship. The authors thank Prof. Yi Cui and Dr. Dusan Coso for helpful discussions.

Author Contributions:

A.D.P. and I.S.M. contributed equally to this work. All authors conceived the experiments and contributed to writing the manuscript. I.S.M. carried out the liquid-phase experiments, and A.D.P. carried out the gas-phase experiments and system modeling.

Competing Interests: the authors declare no competing financial interests.

Supplementary Materials:
Methods
Tables S1 – S3
Figures S1 – S8
Supplementary References (1 - 22)

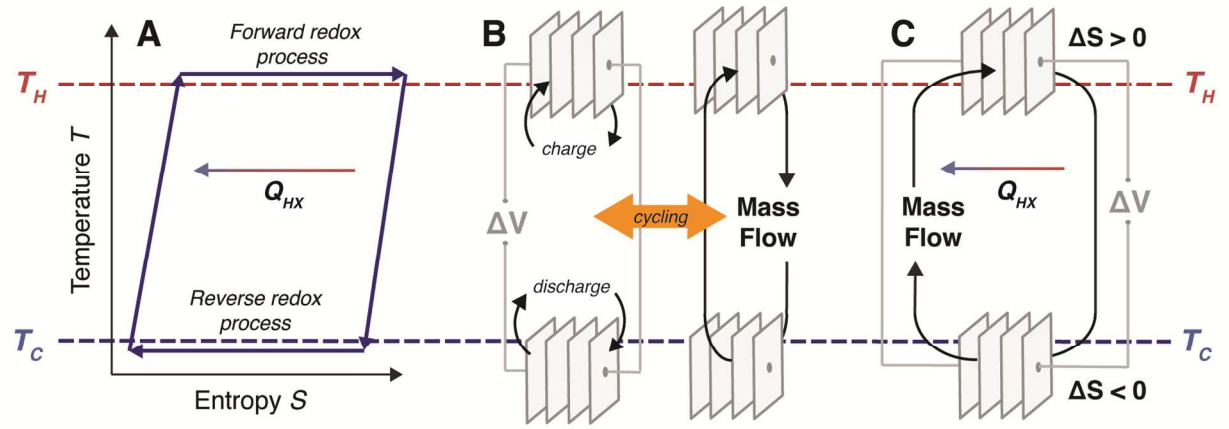

Figure 1 | Continuous electrochemical heat engine. (**a**) temperature-entropy diagram, and system diagrams of the continuous electrochemical heat engine in (**b**) cyclical operation, and (**c**) continuous operation. Two stacks of electrochemical cells are connected in series, one immersed in a hot thermal reservoir at temperature T_H, and the other immersed in a cold thermal reservoir at temperature T_C. The entropy of the electrochemical redox reactions yields a potential difference ΔV across the two stacks of electrochemical cells. The recuperative heat exchange between the two electrolyte streams is shown as Q_{HX}.

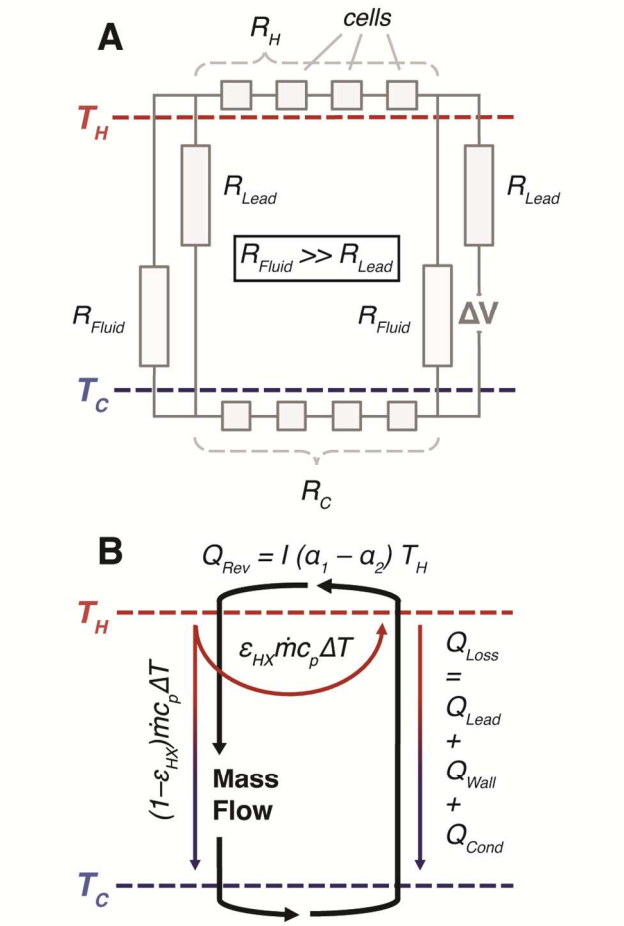

Figure 2 | Electrical and thermal irreversibilities in the continuous electrochemical heat engine. (**a**) Electrical resistances. R_H and R_C are the resistances of stacks of electrochemical cells, R_{Lead} are the resistances of electrical leads spanning between T_H and T_C, and R_{Fluid} is the near-infinite resistance of conduction across the redox-active fluids. In practice, no current flows in the fluids between T_H and T_C. (**b**) Reversible heat input Q_{Rev}, heat leaks, and heat recovery with a heat exchanger.

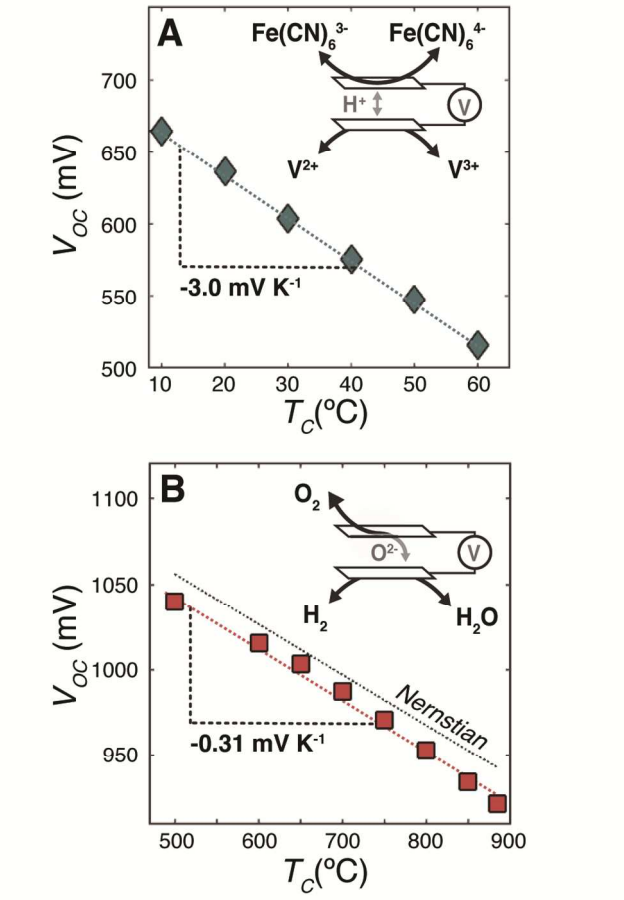

Figure 3 | Open-circuit voltages of electrochemical cells. (**a**) Low-temperature liquid-electrolyte cells used in this study: measured open-circuit potential (V_{OC}) as a function of temperature for a cell consisting of $V^{2+/3+}$ and $Fe(CN)_6^{3-/4-}$ liquid electrolytes with proton exchange through a Nafion membrane. Error bars based on the standard deviation between three sequential measurements are smaller than the marker size. (**b**) High temperature gaseous cells used in this study: V_{OC} as a function of temperature for the water splitting reaction producing H_2 and O_2 with O^{2-} exchange through an oxygen transport membrane using 5% H_2 humidified to $pH_2O \sim 0.028$ atm versus 21% O_2. The error bars, calculated as the deviation of voltage over 30 min, are smaller than the marker size. In both cases, the slope of the line is equivalent to the total thermopower $\alpha_1 - \alpha_2$. The black dotted line in (**b**) shows V_{OC} calculated from thermochemical data with the Nernst equation[46] for comparison.

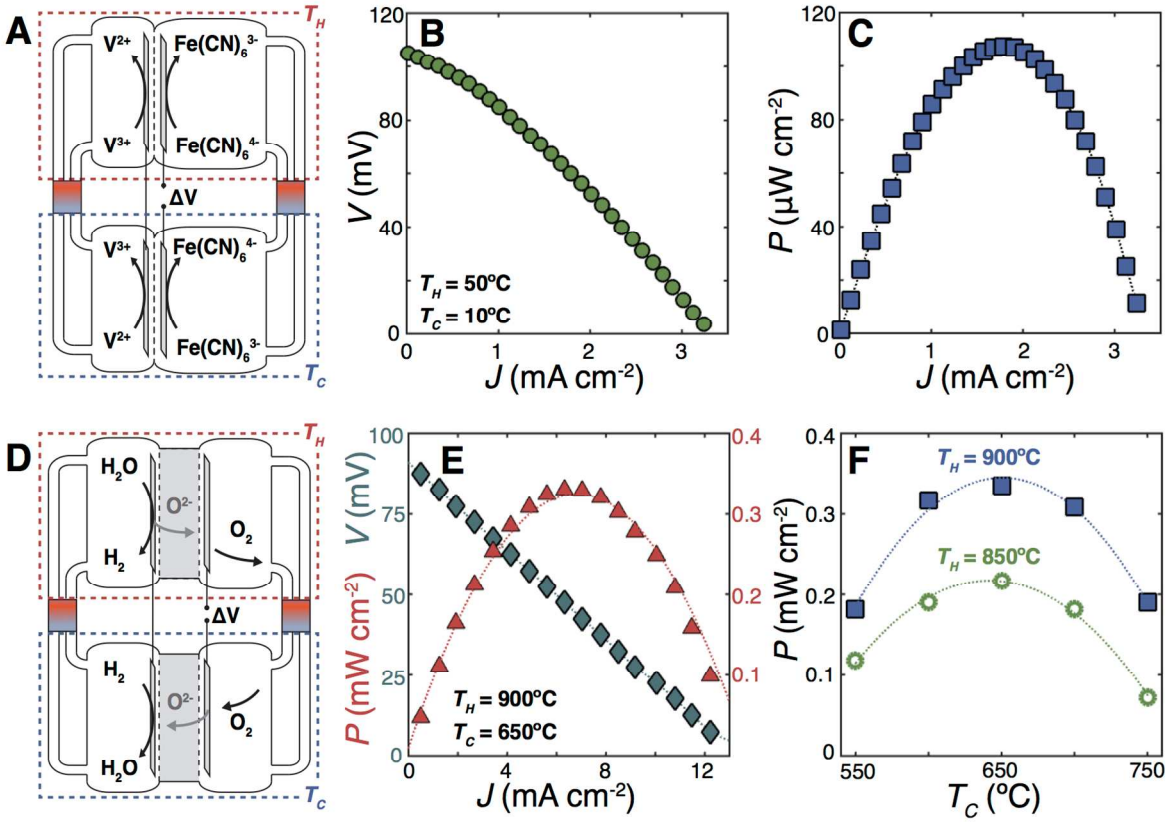

Figure 4 | Two electrochemical heat engines developed in this work. (**a**) Schematic of the low-temperature continuous electrochemical energy harvester based on heat-exchanged flow of electrolyte between two $V^{2+/3+}$||$Fe(CN)_6^{3-/4-}$ cells. Peristaltic pumps used for electrolyte circulation are not shown for clarity. (**b**) Polarization curve for the two $V^{2+/3+}$||$Fe(CN)_6^{3-/4-}$ cells maintained at a ΔT = 40 ºC. While individual dV_{OC}/dT values of low-concentration $V^{2+/3+}$ and $Fe(CN)_6^{3-/4-}$ yield a thermopower as high as 3 mV/K, concentration effects lower the effective thermopower to 2.6 mV/K. (**c**) Power curve produced from the polarization data in (**b**). (**d**) Schematic of a high-temperature electrochemical heat engine using oxygen as the working fluid. The experimental heat engine did not incorporate heat exchange, and continuously exhausted both gases rather than circulating them through the cells. (**e**) Power and polarization characteristic the high-temperature heat engine using 5% H_2 humidified to $pH_2O \sim 0.028$ atm versus 21% O_2, with T_H = 900 °C, T_C = 650 °C. (**f**) Maximum power of the high temperature system as a function of T_C between 550 °C and 750 °C, for T_H = 850 °C (green) and 900 °C (blue). The dotted lines are included as guides for the eye.

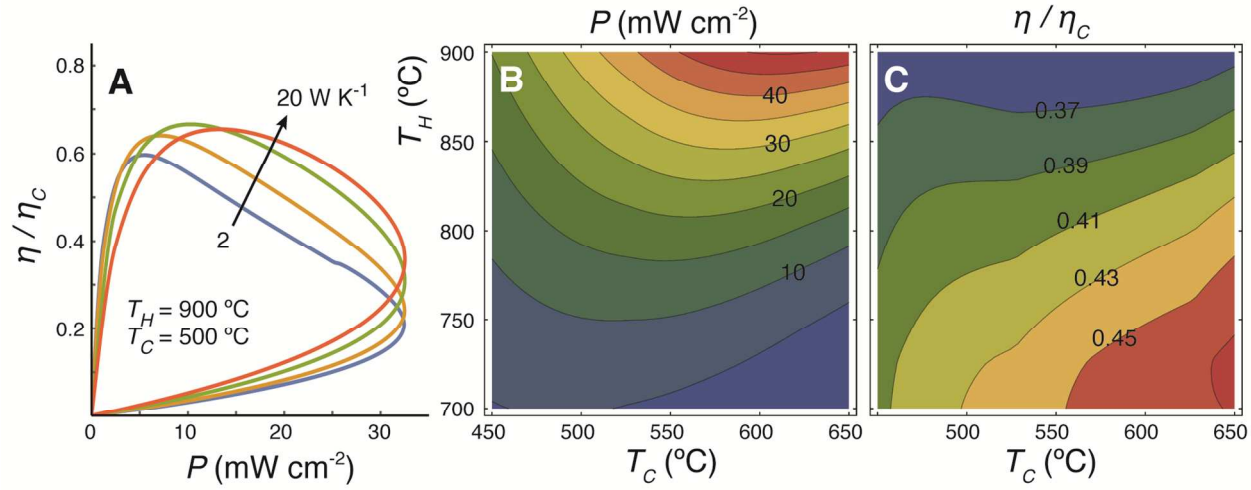

Figure 5 | Simulations of gas-based continuous electrochemical heat engines. (**a**) Efficiency and power parametrized by the current-voltage curves, for a heat engine operating between 900 °C and 500 °C using 90% H_2O and 10% H_2 versus 21% O_2. The four curves correspond to a counterflow heat exchanger rated for 2 (blue), 5 (yellow), 10 (green), and 20 (red) W K^{-1} at 700 °C between the hot and cold cells. (**b**) Maximum power density and (**c**) efficiency at the maximum power point as a function of T_H and T_C for the system corresponding to the red curve in (**a**). Simulations corresponding to panels (**a**)-(**c**) for the near-ambient liquid-based system are shown in Figure S8.

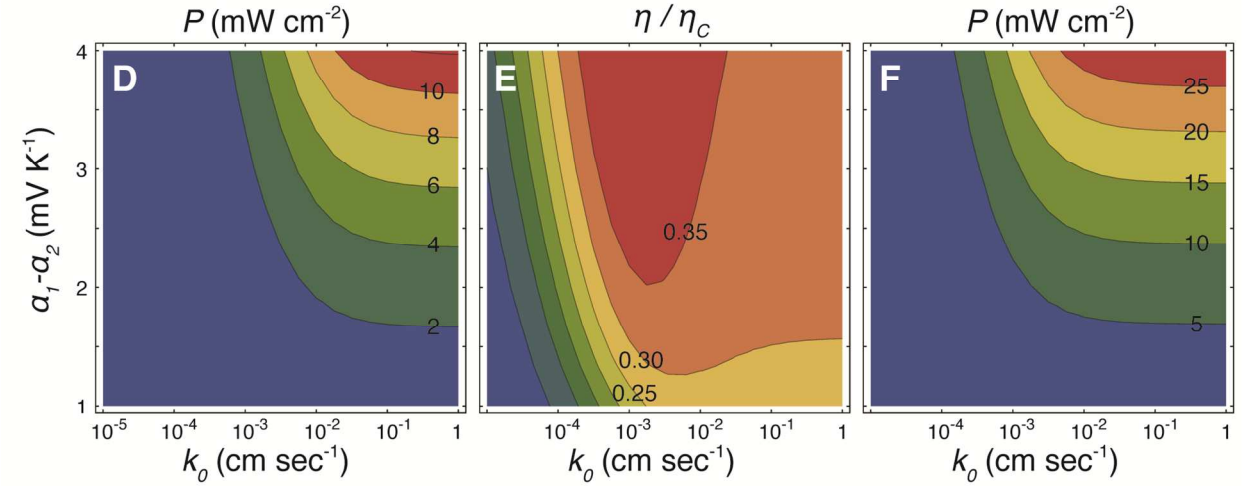

Figure 6 | Simulations of liquid-based continuous electrochemical heat engines. Maximum power density (**a**) and efficiency at the maximum power point (**b**) for a heat engine operating between 50 °C and 10 °C as a function of redox-active fluid properties α and k_0, with concentrations of active species corresponding to the experimental system shown in Figure 4a-c. Corresponding simulations for the high-temperature gas-based system are shown in Figure S3. (**c**) Maximum power density for the same liquid-based electrochemical heat engine as simulated in (**a**) and (**b**), with concentrations of active species increased to 15M.

Redox Couple	α **(mV K^{-1})**
$Fe(CN)_6^{3-/4-}$	-1.4
Benzoquinone/Hydroquinone	-1.1
HBr/Br_2	0.2
Methyl viologen (2+/1+)	0.6
$Fe^{2+/3+}$	1.1
$V^{2+/3+}$	1.7

Table 1. Measured entropy change per coulomb of faradaic charge transfer $\alpha = dE/dT = \Delta S/nF$, for candidate redox couples. Since the device thermopower is the difference α_1-α_2 between the thermopower of two working fluids, the total thermopower can exceed 3 mV K^{-1}.